

# Quantum Anomalous Hall Effect in 2D Organic Topological Insulators

Z. F. Wang, Zheng Liu, and Feng Liu\*  
*Department of Materials Science and Engineering,  
 University of Utah, Salt Lake City, UT 84112, USA*

Quantum anomalous Hall effect (QAHE) is a fundamental transport phenomenon in the field of condensed-matter physics. Without external magnetic field, spontaneous magnetization combined with spin-orbit coupling give rise to a quantized Hall conductivity. So far, a number of theoretical proposals have been made to realize the QAHE, but all based on *inorganic* materials. Here, using first-principles calculations, we predict a family of 2D *organic* topological insulators for realizing the QAHE. Designed by assembling molecular building blocks of triphenyl-transition-metal compounds into a hexagonal lattice, this new class of organic materials are shown to have a nonzero Chern number and exhibit a gapless chiral edge state within the Dirac gap.

PACS numbers: 73.43.-f, 72.20.-i, 81.05.Fb, 72.80.Le

The quantum Hall effect refers to the quantized Hall conductivity due to Landau quantization, as observed in a 2D electron system [1]. The essential ingredient to produce the quantum Hall effect is to break the time-reversal symmetry, usually by applying an external magnetic field. An interesting alternative is to have the internal magnetization coupled with spin-orbit coupling (SOC) that can also break time-reversal symmetry without magnetic field [2]. This is called quantum anomalous Hall effect (QAHE), as first proposed by Haldane [3]. Subsequently, some realistic materials were theoretically proposed to realize the QAHE, such as mercury-based quantum wells [4], graphene [5–7] and topological insulators (TIs) [8]. In general, in a QAHE material, internal magnetism, such as the one induced by transition metals, breaks the time-reversal symmetry and splits the spin degenerated bands. In addition, the SOC opens a global band gap, giving rise to a topologically nontrivial insulating state characterized with the quantized Hall conductivity.

Due to the difficulty in controlling magnetization and SOC, the QAHE has yet to be observed experimentally [9, 10]. So far, all the theoretical proposals for realizing the QAHE are based on inorganic materials. It is fascinating to note that many fundamental physical phenomena in inorganic materials and devices have always found their way to organic counterparts, such as the organic superconductors [11], light-emitting diodes [12], solar cells [13] and field-effect transistors [14]. Therefore, an interesting question is whether the QAHE can be realized in organic materials.

In this Letter, we demonstrate that QAHE can indeed be realized in 2D organic TIs (OTIs) self-assembled from triphenyl-transition-metal compounds, using triphenyl-manganese (TMn) as a model system. Based on Chern number and edge state calculations, we confirm the 2D TMn lattice have nontrivial topological Dirac-gap states and explain the physical origin of its QAHE due to both the intrinsic SOC and strong magnetization provided by Mn atoms.

Our first-principles band structure and band topology calculations were carried out in the framework of the PBE-GGA functional using the VASP package [15]. All self-consistent calculations were performed with a

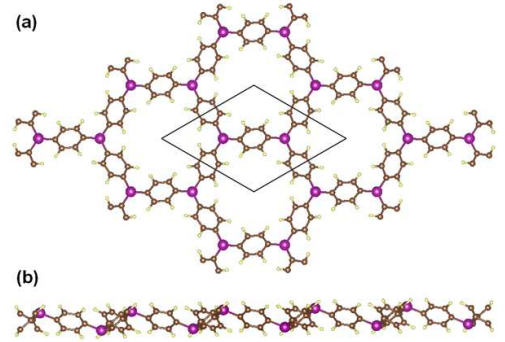


Figure 1: (a) Top and (b) side view of the optimized 2D TMn lattice structure. Rhombus shows the unit cell.

plane-wave cutoff of 500 eV on a  $7 \times 7 \times 1$  Monkhorst-Pack k-point mesh. Supercell with a vacuum layer more than 15 Å thick is used to ensure decoupling between neighboring slabs. For structural relaxation, all the atoms are allowed to relax until atomic forces are smaller than 0.01 eV/Å.

The TMn  $[\text{Mn}(\text{C}_6\text{H}_5)_3]$  molecule consists of a Mn atom bonded with three benzene rings with three-fold rotational symmetry. When bridged with a Mn atom, they may naturally form a 2D hexagonal lattice, as shown in Fig. 1. There are two Mn atoms and three benzene rings with a chemical formula of  $\text{Mn}_2\text{C}_{18}\text{H}_{12}$  in each unit cell and the neighboring benzene rings are bridge-bonded through the para-Mn atoms. The optimized 2D lattice is buckled with the para-Mn atoms moving alternately up and down out of the plane of benzene rings (see Fig. 1b). In addition, each benzene rotates slightly along the Mn-Mn axis in a clockwise manner. The equilibrium lattice constant is found to be 10.7 Å with the Mn-Mn distance and height difference being 6.45 Å and 1.86 Å, respectively.

First, we analyze the band structure of TMn lattice purposely without SOC. The ground state of TMn lattice is found ferromagnetic with a magnetic moment of  $4 \mu_B$  per unit cell, which is 0.18 eV lower than the antiferromagnetic state. The 3d-shell of Mn is half filled, after providing three d electrons to bond with the C, each Mn atom is left with two unpaired d electrons of

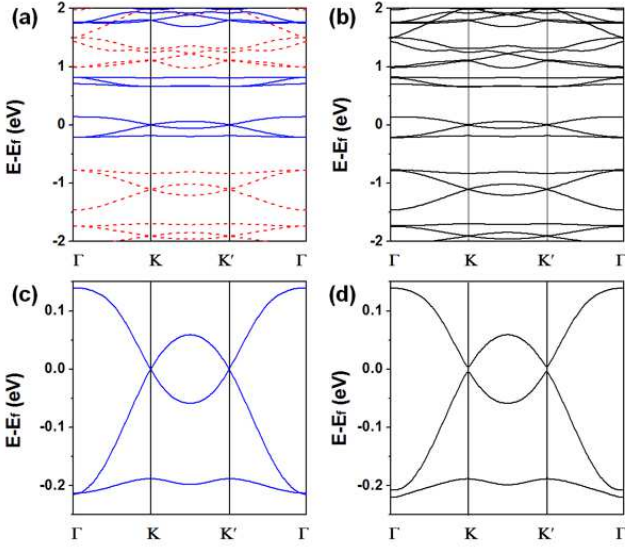


Figure 2: (a) and (b) Band structures of the TMn lattice without and with SOC, respectively. Red dashed lines and blue solid lines denote spin-up and spin-down bands. (c) and (d) Magnification of (a) and (b) around the Fermi level, respectively.

the same spin. The band structure of the ferromagnetic state is shown in Fig. 2(a). Due to internal magnetization, the spin-up (red dashed line) and spin-down (blue solid line) bands are completely split away from each other, and only the spin-down band is left around the Fermi level (a half semimetal). Magnifying the bands around the Fermi level, we can see a clear linear Dirac band, with the Fermi level located exactly at the Dirac point ( $K$  and  $K'$ ), as shown in Fig. 2(c). Similar spin-up Dirac bands are below the Fermi level. Next, the SOC is included, and the corresponding band structure is shown in Fig. 2(b). Our magnetic anisotropy calculation shown that the SOC ground state has the out-of-plane spin orientation, which is 0.5 meV lower than the in-plane spin orientation. Comparing Fig. 2(b) to Fig. 2(a), they are almost the same, except a sizable bulk band gap (9.5 meV) opened at  $K$  and  $K'$  Dirac points around Fermi level, which can be seen more clearly from the magnified band in Fig. 2(d) compared to Fig. 2(c).

We checked that the Dirac states mainly come from the Mn d orbit, with little contribution from the C p orbit, as shown in Fig. 3(a). Therefore, the Dirac band around the Fermi level originates from the hexagonal Mn lattice. To identify the topological properties of the Dirac gap, we calculated the Berry curvature of the bands using the Kubo formula [16, 17],

$$\Omega(\mathbf{k}) = \sum_n f_n \Omega_n(\mathbf{k}),$$

$$\Omega_n(\mathbf{k}) = - \sum_{n' \neq n} 2Im \frac{\langle \psi_{n\mathbf{k}} | v_x | \psi_{n'\mathbf{k}} \rangle \langle \psi_{n'\mathbf{k}} | v_y | \psi_{n\mathbf{k}} \rangle}{(\varepsilon_{n'\mathbf{k}} - \varepsilon_{n\mathbf{k}})^2}, \quad (1)$$

where  $n$  is the band index,  $\varepsilon_{n\mathbf{k}}$  and  $\psi_{n\mathbf{k}}$  are eigenvalue and eigenstate of band  $n$ , respectively,  $v_{x/y}$  is the velocity operator,  $f_n$  is Fermi distribution function. We

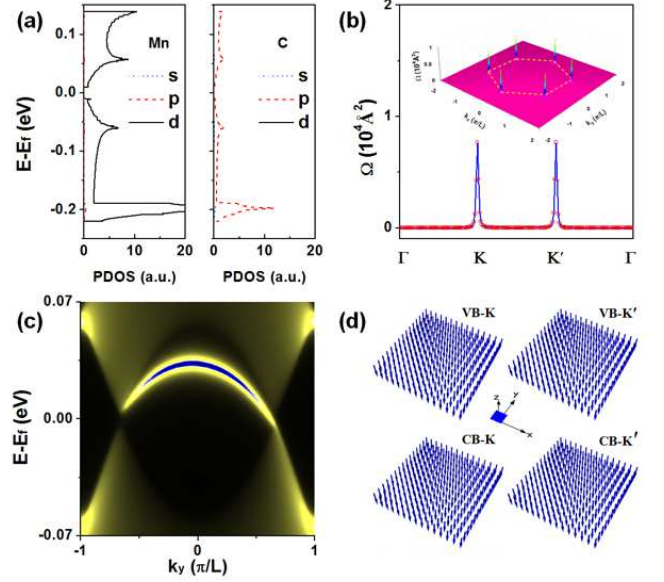


Figure 3: (a) Projected density of states of Dirac bands around the Fermi level. (b) Berry curvature for the whole valence bands (blue solid line) and the highest occupied valence band below the Fermi level (red open circle) along the high-symmetry directions. Inset: the 2D distribution of berry curvature for the whole valence bands in the momentum space. The first Brillouin zone is denoted by the dashed line. (c) Semi-infinite edge states inside the Dirac gap of the TMn lattice. (d) 3D spin texture round  $K$  and  $K'$  for the highest occupied valence band and the lowest unoccupied conduction band.

have used the maximally localized Wannier functions (MLWFs) to calculate the Berry curvature by using the Wannier90 package [18]. The inner energy window used to accurately reproduce the first-principles bands is set from  $E_f - 8.0$  eV to  $E_f + 3.0$  eV. Fig. 3(b) shows the Berry curvature for the whole valence bands (blue solid line) along the high-symmetry directions and the corresponding 2D distribution in momentum space (inset). We see that the nonzero Berry curvatures are localized around  $K$  and  $K'$  points with the same sign. Integrating the Berry curvatures over the first Brillouin zone, we obtain the Chern number,  $C = \frac{1}{2\pi} \int_{BZ} d^2k \Omega = 1$ , with each Dirac cone ( $K$  and  $K'$ ) contributing 0.5. Such nonvanishing Chern number characterizes a quantized Hall conductivity and confirms the QAHE in the TMn lattice.

The nonzero Chern number can also be manifested by the presence of chiral edge states within the topological nontrivial Dirac gap. By using the MLWFs obtained from the first-principles calculation, the edge Green's function [19] of the semi-infinite TMn lattice is constructed and the local density of state (LDOS) of edge states are calculated [20, 21], as shown in Fig. 3(c) for one of the edges (the LDOS of the other edge state is symmetric to this one). The number of the edge states indicates the absolute value of the Chern number. Apparently, the one chiral edge state observed in the Dirac gap is consistent with the calculated Chern

number  $C = 1$ .

To better understand the odd Chern number  $C = 1$ , the Berry curvature for the highest occupied valence band (VB) below the Fermi level is also calculated, as shown in Fig. 3(b) (red open circle), which completely matches the total Berry curvature curve. This indicates that the sum of Chern number for other valence bands below the highest occupied valence band is zero. Thus, we can focus on the highest occupied valence band only, and examine its spin components around the Dirac gap. As a comparison, the lowest unoccupied conduction band (CB) above the Fermi level is also studied. As shown in Fig. 3(d), the spin textures for VB and CB are uniformly pointing along the  $-z$  direction around  $K$  and  $K'$ , as both come from the spin-down bands. Qiao *et al.* [6] recently showed that such spin texture has no contribution to the Chern number, but the pseudo-spin texture of the Dirac states may contribute to the Chern number. To see whether the nontrivial topology of our TMn lattice is also originated from the pseudo-spin texture, we construct a tight-binding (TB) model, as follows.

Since our TMn lattice has inversion symmetry, the gap opening at the Dirac point cannot be induced by the Rashba SOC as in the doped graphene [5–7], but instead by the intrinsic SOC of Mn atoms. To further illustrate the intrinsic SOC effect, we write a single  $\pi$ -band TB model to describe the Dirac bands of hexagonal TMn lattice. To the first-order approximation, the TB Hamiltonian with exchange field and intrinsic SOC can be written as,

$$H = t \sum_{\langle i,j \rangle, \alpha} c_{i\alpha}^+ c_{j\alpha} - M \sum_{i, \alpha, \beta} c_{i\alpha}^+ s_{\alpha\beta}^z c_{i\beta} + \lambda_{so} \frac{2i}{\sqrt{3}} \sum_{\langle\langle i,j \rangle\rangle} c_i^+ \vec{s} \cdot (\vec{d}_{kj} \times \vec{d}_{ik}) c_j. \quad (2)$$

Here,  $c_{i\alpha}^+$  and  $c_{i\alpha}$  are  $\pi$ -band creation and annihilation operators, respectively, for an electron with spin  $\alpha$  on site  $i$ . The first term is the nearest-neighbor hopping with magnitude  $t$ . The second term is the exchange field with magnitude  $M$ . The third term is the next-nearest-neighbor intrinsic SOC with amplitude  $\lambda_{so}$ ,  $\vec{s}$  is the spin Pauli matrix,  $\vec{d}_{kj}$  is the unit vector pointing from site  $j$  to  $k$ . We note that this intrinsic SOC term forbids mixing of spin-up and spin-down states due to its special nature of 2D geometry, a condition that will breakdown if the structure is not perfect 2D.

Diagonalizing the above Hamiltonian in reciprocal space, we obtain its band structure, as shown in Fig. 4. In our calculation, all the parameters are scaled with the hopping parameter  $t$ . Without SOC and exchange field, the corresponding band structure along the high-symmetry directions is shown in Fig. 4(a), where we can see the linear Dirac bands at  $K$  and  $K'$  points. When we turn on the SOC but without the exchange field, a band gap is opened at the Dirac points, as shown in Fig. 4(b). Without the exchange field, all the bands are spin degenerated in Fig. 4(b). When we turn on both SOC and exchange field, the spin de-

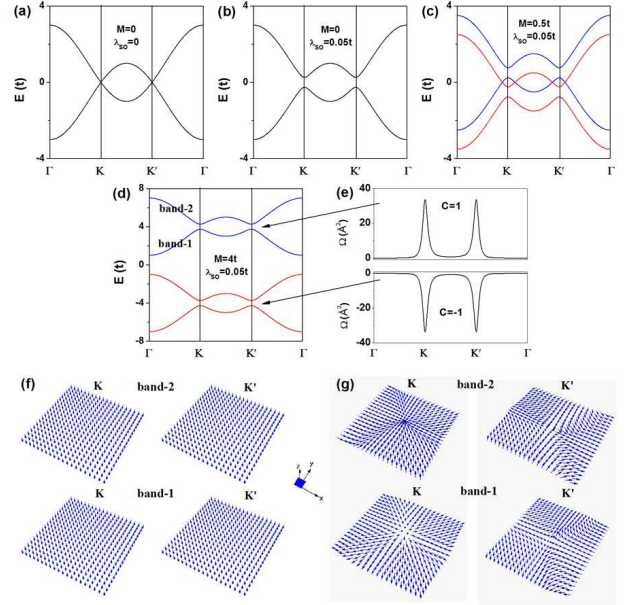


Figure 4: TB Band structure with (a)  $M=0$  and  $\lambda_{so}=0$ , (b)  $M=0$  and  $\lambda_{so}=0.05t$ , (c)  $M=0.5t$  and  $\lambda_{so}=0.05t$  and (d)  $M=4t$  and  $\lambda_{so}=0.05t$ . (e) Berry curvatures by setting the Fermi level within the intrinsic SOC gap indicated by the arrows and the resulting Chern numbers. Red (blue) color denotes spin-up (spin-down) bands. (f) and (g) 3D spin and pseudo-spin texture around  $K$  and  $K'$  for band-1 and band-2 shown in (d).

generacy is lifted. If the exchange field is large enough to overcome the SOC gap, the spin-up (red line) and spin-down (blue line) bands will cross over with each other, as shown in Fig. 4(c). The situation here, however, is different from the case of Rashba SOC in doped graphene [5–7], as there is no SOC gap opening at the band crossing points with different spins in the physical regime of small magnetization. However, if we further increase the exchange field, the spin-up and spin-down bands will completely separate from each other, as shown in Fig. 4(d), which corresponds to our case of TMn lattice. Then, we have a global gap induced by intrinsic SOC, leading to QAHE. To further check the topological properties of the gap states induced by intrinsic SOC, we calculated the Berry curvature by setting the Fermi level inside the spin-up and spin-down Dirac gap, respectively (The real TMn lattice has the Fermi level in the gap of spin-down bands). The corresponding Berry curvature and Chern number are shown in Fig. 4(e). We found the non-zero Berry curvature that localizes around the Dirac point and the  $C = -1$  ( $C = 1$ ) for spin-up (spin-down) bands, consistent with our first principles calculations. Thus, we confirm that the intrinsic SOC in TMn lattice is responsible for gap opening to realize the QAHE.

To reveal the difference between spin and pseudo-spin, we calculate the Chern number (topological charge) resulting from the spin and pseudo-spin texture separately, using the the TB model. The spin and pseudo-spin components are defined as [6]  $\langle s_i \rangle =$

$\langle \psi | I \otimes s_i | \psi \rangle$  and  $\langle \sigma_i \rangle = \langle \psi | \sigma_i \otimes I | \psi \rangle$ , respectively, where  $I$  is a  $2 \times 2$  identity matrix,  $s_i$  ( $\sigma_i$ ) is the spin (pseudo-spin) Pauli matrix with  $i = x, y, z$  and  $|\psi\rangle$  is the eigenvector of Eq. (2) in reciprocal space. Here, we choose the spin-down bands labeled with band-1 and band-2 in Fig. 4(d) for our calculation, as our first-principles calculations show only spin-down bands at the Fermi Level [Fig. 2(a)]. Fig. 4(f) shows the TB spin texture with all spins uniformly pointing along the  $-z$  direction, consistent with the first-principles results [Fig. 3(d)]. However, the pseudo-spin texture is not uniform, as shown in Fig. 4(g). Its in-plane components have different patterns depending on the valleys ( $K$  and  $K'$ ) and bands (band-1 and band-2), while its out-of-plane components only exist near the valley and point along either  $-z$  or  $z$  direction. The spin and pseudo-spin Chern number can be calculated as [6, 22]  $n = 1/4\pi \int dk^2 (\partial_{k_x} \hat{\mathbf{h}} \times \partial_{k_y} \hat{\mathbf{h}}) \cdot \hat{\mathbf{h}}$ , where  $\hat{\mathbf{h}} = \mathbf{h}/|\mathbf{h}|$  with  $\mathbf{h}$  representing the projection of Hamiltonian in Eq. (2) into spin or pseudo-spin space. Physically, the unit vector  $\hat{\mathbf{h}}$  represents the expectation value of the orientation of the spin or pseudo-spin associated with the eigenvector  $|\psi\rangle$ . For band-1 in Fig. 4(d), we found  $n_{spin}=0$  and  $n_{pseudo} = 0.5$  for both valleys. The pseudo-spin texture provides a half topological charge, corresponding to a meron. Thus, by counting two valleys' contribution, the Chern number  $C = 1$ . In addition, the sign of the topological charge is determined by the details of the pseudo-spin texture. For band-2 in Fig. 4(d), we found  $n_{spin}=0$  and  $n_{pseudo} = -0.5$  for both valleys. Therefore, the total Chern number for band-1 and band-2 is zero, which is consistent with our first-principles result.

Besides realizing the QAHE in a new organic molecular lattice, it is important to point out some new physics in our system in comparison with previous works. The QAHE in our proposed TMn lattice has an odd Chern number ( $C = 1$ ) which is induced by intrinsic SOC taking place in the strong magnetization regime, while the QAHE in the transition metal doped graphene has an even Chern number ( $C = 2$ ) which is induced by Rashba SOC taking place in the weak magnetization regime. It was shown that the d-states in 5d transition metal doped graphene plays a determining role in realizing the QAHE and there exists also a global Dirac gap between the bands of the same spin [Fig. 2(c) in Ref. 7], but it is 0.27 eV below the Fermi level and its Chern number is even ( $C = -2$ ).

Lastly, one critical point is whether the topological properties of TMn lattice can remain on a substrate. Naturally one should look for a substrate with minimal interfacial interaction with the TMn lattice. To test

out this possibility, we have placed the TMn lattice on top of graphene [Fig. S1(a)] [23], which is expected to have a weak van der Waals interfacial interaction and right hexagonal symmetry. Our calculations show that because of lattice mismatch, the TMn lattice becomes a flat structure instead of the freestanding buckled structure, but the main features of QAHE remain intact. There is still a SOC gap at the Dirac point around Fermi level [Figs. S1(e) and (f)], within which a nontrivial topological edge state resides [Fig. S1(g)]. These results demonstrate the feasibility of attaining the QAHE of TMn lattice on a substrate.

This work was supported by US DOE-BES (Grant No. DE-FG02-04ER46148) and NSF MRSEC (Grant No. DMR-1121252). Z.F.W. acknowledges additional support from ARL (Cooperative Agreement No. W911NF-12-2-0023). We thank the CHPC at University of Utah and NERSC for providing the computing resources.

---

\* Corresponding author. E-mail: fliu@eng.utah.edu

- [1] K. V. Klitzing *et al.*, Phys. Rev. Lett. **45**, 494 (1980).
- [2] N. Nagaosa *et al.*, Rev. Mod. Phys. **82**, 1539 (2010).
- [3] F. D. M. Haldane, Phys. Rev. Lett. **61**, 2015 (1988).
- [4] C.-X. Liu *et al.*, Phys. Rev. Lett. **101**, 146802 (2008).
- [5] Z. Qiao *et al.*, Phys. Rev. B **82**, 161414(R) (2010).
- [6] Z. Qiao *et al.*, Phys. Rev. B **85**, 115439 (2012).
- [7] H. Zhang *et al.*, Phys. Rev. Lett. **108**, 056802 (2012).
- [8] R. Yu *et al.*, Science **329**, 61 (2010).
- [9] C.-Z. Chang *et al.*, arXiv:1108.4754v1.
- [10] J. G. Checkelsky *et al.*, Nature Phys. **8**, 729 (2012).
- [11] D. Jérôme *et al.*, J. Phys. Lett. (Paris) **41**, L95 (1980).
- [12] C. W. Tang and S. A. Vanslyke, Appl. Phys. Lett. **51**, 913 (1987).
- [13] D. Kearns and M. Calvin, J. Chem. Phys. **29**, 950 (1958).
- [14] H. Koezuka, A. Tsumura and T. Ando, Synth. Met. **18**, 699 (1987).
- [15] G. Kresse and J. Hafner, Phys. Rev. B **47**, 558 (1993).
- [16] D. J. Thouless *et al.*, Phys. Rev. Lett. **49**, 405 (1982).
- [17] Y. Yao *et al.*, Phys. Rev. Lett. **92**, 037204 (2004).
- [18] A. A. Mostofi *et al.*, Comput. Phys. Commun. **178**, 685 (2008).
- [19] M. P. Lopez Sancho *et al.*, J. Phys. F **15**, 851 (1985).
- [20] Z. F. Wang, Z. Liu and F. Liu, Nature Commun. **4**, 1471 (2013).
- [21] Z. Liu *et al.* Phys. Rev. Lett. **110**, 106804 (2013).
- [22] E. Prada *et al.*, Solid State Comm. **151**, 1075 (2011).
- [23] See Supplemental Material at the [http://link.aps.org/supplemental/\\*\\*/](http://link.aps.org/supplemental/**/) for more information on the substrate effect.